

Gapless and ordered phases in spin-1/2 Kitaev-XX-Gamma chain

Zebin Zhuang(庄泽彬) and Wang Yang(杨望)
Citation: Chin. Phys. B, 2026, 35 (**3**): 037503. DOI: 10.1088/1674-1056/ae3067
http://cpb.iphy.ac.cn; http://iopscience.iop.org/cpb

What follows is a list of articles you may be interested in

Spin gap in quasi-one-dimensional *S*=3/2 antiferromagnet $CoTi_2O_5$

Hao-Hang Xu(徐浩航), Qing-Yuan Liu(刘庆元), Chao Xin(辛潮), Qin-Xin Shen(申沁鑫), Jun Luo(罗军), Rui Zhou(周睿), Jin-Guang Cheng(程金光), Jian Liu(刘健), Ling-Ling Tao(陶玲玲), Zhi-Guo Liu(刘志国), Ming-Xue Huo(霍明学), Xian-Jie Wang(王先杰), and Yu Sui(隋郁)
Chin. Phys. B, 2024, 33 (**3**): 037505. DOI: 10.1088/1674-1056/ad1381

Off-diagonal approach to the exact solution of quantum integrable systems

Yi Qiao(乔艺), Junpeng Cao(曹俊鹏), Wen-Li Yang(杨文力), Kangjie Shi(石康杰), and Yupeng Wang(王玉鹏)
Chin. Phys. B, 2023, 32 (**11**): 117504. DOI: 10.1088/1674-1056/ad0774

Exact surface energy and elementary excitations of the *XXX* spin-1/2 chain with arbitrary non-diagonal boundary fields

Jia-Sheng Dong(董家生), Pengcheng Lu(路鹏程), Pei Sun(孙佩), Yi Qiao(乔艺), Junpeng Cao(曹俊鹏), Kun Hao(郝昆), and Wen-Li Yang(杨文力)
Chin. Phys. B, 2023, 32 (**1**): 017501. DOI: 10.1088/1674-1056/ac981f

Low-temperature heat transport of the zigzag spin-chain compound $SrEr_2O_4$

Liguo Chu(褚利国), Shuangkui Guang(光双魁), Haidong Zhou(周海东), Hong Zhu(朱弘), and Xuefeng Sun(孙学峰)
Chin. Phys. B, 2022, 31 (**8**): 087505. DOI: 10.1088/1674-1056/ac5e97

Dynamical signatures of the one-dimensional deconfined quantum critical point

Ning Xi(西宁) and Rong Yu(俞榕)
Chin. Phys. B, 2022, 31 (**5**): 057501. DOI: 10.1088/1674-1056/ac5987

Gapless and ordered phases in spin-1/2 Kitaev–XX–Gamma chain

Zebin Zhuang(庄泽彬)[1] and Wang Yang(杨望)[2,†]

[1] *Department of Physics, Imperial College London, London SW7 2BZ, UK*
[2] *School of Physics, Nankai University, Tianjin* 300071, *China*

(Received 26 September 2025; revised manuscript received 1 December 2025; accepted manuscript online 23 December 2025)

We study the spin-1/2 Kitaev chain with additional XX and symmetric off-diagonal Gamma interactions. By combining the Jordan–Wigner transformation with density matrix renormalization group (DMRG) numerical simulations, we obtain the exact solution of the model and map out the phase diagram containing six distinct phases. The four gapped phases display ferromagnetic and antiferromagnetic magnetic orders along the $(1,1,0)$- and $(1,-1,0)$-spin directions, whereas in the gapless phases, the low-energy spectrum consists of two branches of helical Majorana fermions with unequal velocities. The transition lines separating different phases include deconfined quantum critical lines with dynamical critical exponent $z=1$ and quadratic critical lines with $z=2$. Our work reveals the rich interplay among symmetry, magnetic order, and quantum criticality in the Kitaev–XX–Gamma chain.

Keywords: spin chain, magnetism, magnetic phase transition, quantum compass model

PACS: 75.10.Pq

DOI: 10.1088/1674-1056/ae3067 **CSTR:** 32038.14.CPB.ae3067

1. Introduction

Quantum compass models[1] are an important class of spin models where magnetic exchange interactions favor different spin components on different bonds, sitting at the crossroads of spin–orbital physics and strongly correlated quantum magnetism. One-dimensional (1D) spin-1/2 quantum compass models are of special interest because of their often exact solvability via dualities and Jordan–Wigner transformations, which makes possible an analytical understanding of various physical properties of the system, including the excitation spectrum, correlation functions, and entanglement entropies, to name a few.[2–18] A typical quantum compass model in 1D is Kitaev's exactly solvable spin-1/2 model, which has bond-dependent Ising interactions with two-site periodicity and an exponentially large ground-state degeneracy.[2]

Recently, there has been increasing research interest in the effects of an off-diagonal symmetric Gamma interaction $S_i^x S_j^y + S_i^y S_j^x$,[19] which couples orthogonal spin directions, unlike the Ising type of interactions that couple the same spin components. The inclusion of the off-diagonal Gamma interaction is often indispensable when studying strongly correlated spin–orbit-coupled magnets with edge-sharing octahedra, where the interplay between strong spin–orbit coupling and crystal fields leads to anisotropy in magnetic exchange interactions.[20–25] Therefore, the Gamma interaction is considered a "real-world" correction to pure Kitaev/compass physics. In 1D, Ising and XY chains with an additional Gamma term have been considered, in which rich physics including quantum phase transitions, quantum criticality, entanglement, and information scrambling have been investigated.[26–33] However, the 1D quantum compass model augmented with a Gamma term remains less explored. A prototypical example of such a 1D compass–Gamma model is the spin-1/2 Kitaev–XX–Gamma chain, which will be the focus of this work.

It is worth noting that besides the above discussions, the consideration of the 1D compass–Gamma model is also motivated from a two-dimensional (2D) perspective, since in certain circumstances, 1D studies can provide insights into understanding 2D physics. The Kitaev spin-1/2 model on the honeycomb lattice[34] is an exactly solvable quantum compass model in 2D, which hosts fractionalized anyonic excitations that can be used for realizing fault-tolerant topological quantum computation.[34,35] Real materials, however, inevitably host additional spin interactions allowed by lattice symmetries, which spoil the exact solvability of the Kitaev honeycomb model and complicate the model both analytically and numerically.[19,20,36,37] In particular, the off-diagonal Gamma interaction has been shown to exist in real Kitaev materials with an interaction strength even comparable with the dominant Kitaev interaction, and a typical model for describing 2D real Kitaev materials is the Kitaev–Heisenberg–Gamma model.

A productive route to a controlled understanding of the 2D case is to descend to 1D generalizations of the Kitaev model — obtained by restricting the honeycomb network to a chain and supplementing it with symmetry-allowed terms.[38–58] Despite their simplicity, these systems exhibit rich intrinsic physics, including nonsymmorphic symmetry

†Corresponding author. E-mail: wyang@nankai.edu.cn

© 2026 Chinese Physical Society and IOP Publishing Ltd. All rights, including for text and data mining, AI training, and similar technologies, are reserved.

group structures,[38] nonlocal string orders,[38] and solitonic excitations.[39,40] Moreover, weakly coupled Kitaev chains can reconstruct hallmark 2D orders (e.g., zigzag and stripy magnetism[41]), thereby furnishing a quasi-1D bridge back to 2D Kitaev materials. We note that the 1D Kitaev–XX–Gamma model considered in this work has a similar symmetry group as the Kitaev–Heisenberg–Gamma model. The exact solvability of the spin-1/2 Kitaev–XX–Gamma chain makes a more thorough and comprehensive theoretical study possible, compared with the non-exactly-solvable Kitaev–Heisenberg–Gamma model.

In recent years, interest in one-dimensional quantum compass/Kitaev-type spin chains has been driven not only by their exact solvability and rich quantum critical behavior, but also by growing experimental motivation from real materials. In particular, the literature[59] demonstrated via THz spectroscopy that the quasi-1D magnet $CoNb_2O_6$ is not simply described by the transverse-field Ising chain; instead, it realizes a bond-dependent "twisted Kitaev chain". Their work shows that bond-anisotropic interactions induced by spin–orbit coupling and crystal symmetry can generate nontrivial domain-wall dynamics, thereby directly linking 1D Kitaev/compass physics to Co^{2+}-based materials. Inspired by this, we further consider a more realistic scenario relevant to edge-sharing octahedral magnets and study a 1D Kitaev chain augmented by symmetry-allowed off-diagonal Γ interactions and an additional XX exchange as "realistic corrections".

In this work, we focus on the 1D spin-1/2 Kitaev–XX–Gamma model, which is an exactly solvable 1D quantum compass–Gamma model via the Jordan–Wigner transformation. By combining the Jordan–Wigner solution with DMRG numerical simulations, a variety of gapless and gapped phases are revealed, occupying extended regions in the phase diagram. As shown in Fig. 1, we find that the gapped phases have ferromagnetic (FM) and antiferromagnetic (AFM) orders along the $(1,1,0)$- and $(1,-1,0)$-directions in spin space, depending on the parameter regions; whereas the gapless phases possess a low-energy spectrum consisting of two branches of helical Majorana fermions with distinct velocities. For the phase transitions, the two AFM phases (similarly for the FM phases) are separated by a line of critical points with vanishing Gamma interaction; hence this critical line constitutes an example of a deconfined quantum phase transition in 1D. On the other hand, the critical lines separating the gapped phases from the gapless regions have a quadratic low-energy dispersion, with dynamical critical exponent $z = 2$.

The rest of the paper is organized as follows. In Section 2, the model Hamiltonian is introduced and the associated symmetries are discussed. In Section 3, we apply the Jordan–Wigner transformation to exactly diagonalize the Hamiltonian and analyze the dispersion to delineate different phases. Section 4 is devoted to a numerical study of the phase diagram, in which ground-state degeneracies, correlation functions, and central charges are calculated. Section 5 briefly summarizes the main results of the paper.

2. Model Hamiltonian and symmetries

2.1. Model Hamiltonian

We consider the 1D spin-1/2 Kitaev–XX–Gamma model defined by the following Hamiltonian:

$$H = \sum_{\langle ij\rangle\in\gamma\,\text{bond}} \left[K S_i^\gamma S_j^\gamma + J(S_i^x S_j^x + S_i^y S_j^y) + \Gamma(S_i^x S_j^y + S_i^y S_j^x)\right], \tag{1}$$

in which i, j denote two nearest-neighbor sites; $\gamma = x, y$ is the spin direction associated with the γ bond connecting nearest-neighbor sites i and j, with the pattern shown in Fig. 2; K, J, and Γ denote the Kitaev, XX, and symmetric off-diagonal Gamma couplings, respectively.

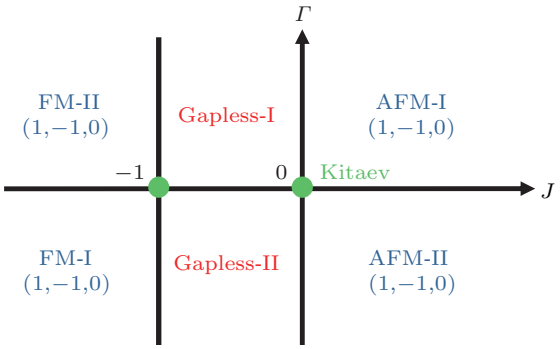


Fig. 1. Phase diagram of the 1D spin-1/2 Kitaev–XX–Gamma model with $K = 1$. AFM-I and FM-I denote antiferromagnetic and ferromagnetic phases polarized along the spin direction $(1,1,0)$, whereas AFM-II and FM-II denote the corresponding phases along $(1,-1,0)$. At the parameter points $(0,0)$ and $(-1,0)$, the model reduces to the pure Kitaev chain.

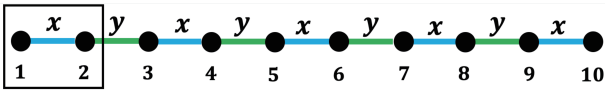


Fig. 2. Bond pattern of the Kitaev–XX–Gamma chain.

Since the special case $K = 0$ has already been studied in Refs. [31,32], we restrict our analysis to the case $K \neq 0$. It is important to note that the two standard choices $K = \pm 1$ are related by a unitary two-sublattice rotation U_2, defined as

$$\begin{aligned} &\text{Sublattice 1}: \ (x,y,z) \to (-x',-y',z'),\\ &\text{Sublattice 2}: \ (x,y,z) \to (x',y',z'), \end{aligned} \tag{2}$$

where a spin rotation about $\hat{z}$ by an angle π is applied to every even site, while the odd sites are left unchanged. The Hamiltonian then transforms as $H' = U_2 H U_2^{-1}$, which can be made explicit in the first unit cell containing sites 1 and 2 as follows:

$$\begin{aligned} H'_{12} &= -K S_1^x S_2^x - J(S_1^x S_2^x + S_1^y S_2^y) - \Gamma(S_1^x S_2^y + S_1^y S_2^x),\\ H'_{23} &= -K S_2^y S_3^y - J(S_2^x S_3^x + S_2^y S_3^y) - \Gamma(S_2^x S_3^y + S_2^y S_3^x). \end{aligned} \tag{3}$$

Therefore, the U_2 rotation establishes an equivalence relation in parameter space

$$(K,J,\Gamma) \simeq (-K,-J,-\Gamma). \tag{4}$$

For a non-standard choice of K, we can map the parameters to the standard cases by redefining Γ and J according to the substitutions $\Gamma \to \Gamma/K$ and $J \to J/K$. Hence, because of the equivalence relation in Eq. (4) and the rescaling of Γ and J, without loss of generality we can always fix $K = 1$, and it suffices to study the parameter space spanned by (J,Γ).

Consider the global spin rotation $R(\hat{x},\pi)$ applied to every site, where $R(\hat{n},\varphi)$ denotes a global spin rotation around the direction $\hat{n}$ by an angle φ. Clearly, $R(\hat{x},\pi)$ flips S_i^y to $-S_i^y$ ($1 \le i \le N$, where N is the number of sites), and as a result this operation only changes the sign of the Γ coupling, implying the following equivalence relation:

$$(K,J,\Gamma) \simeq (K,J,-\Gamma). \tag{5}$$

Next, we consider another two-sublattice rotation U_2', defined as

$$\begin{aligned} &\text{Sublattice 1: } (x,y,z) \longrightarrow (-y',x',z'),\\ &\text{Sublattice 2: } (x,y,z) \longrightarrow (y',-x',z'), \end{aligned} \tag{6}$$

which corresponds to applying the spin rotation around the z-direction by an angle $\pi/2$ ($-\pi/2$) to every odd (even) site. The transformed Hamiltonian in the first unit cell is then given by

$$\begin{aligned} H_{12}' &= KS_1^xS_2^x-(J+K)(S_1^xS_2^x+S_1^yS_2^y)\\ &\quad +\Gamma(S_1^xS_2^y+S_1^yS_2^x),\\ H_{23}' &= KS_2^yS_3^y-(J+K)(S_2^xS_3^x+S_2^yS_3^y)\\ &\quad +\Gamma(S_2^xS_3^y+S_2^yS_3^x), \end{aligned} \tag{7}$$

which reveals the following equivalence relation

$$(K,J,\Gamma) \simeq (K,-K-J,\Gamma). \tag{8}$$

2.2. Hamiltonian symmetries

The Hamiltonian in Eq. (1) is invariant under the following transformations:

$$\begin{aligned} T &: (S_i^x,S_i^y,S_i^z) \to (-S_i^x,-S_i^y,-S_i^z),\\ R(\hat{z},\pi) &: (S_i^x,S_i^y,S_i^z) \to (-S_i^x,-S_i^y,S_i^z),\\ R(\hat{n}_1,\pi)I &: (S_i^x,S_i^y,S_i^z) \to (-S_{2-i}^y,-S_{2-i}^x,-S_{2-i}^z),\\ R(\hat{n}_1,\pi)T_a &: (S_i^x,S_i^y,S_i^z) \to (-S_{i+1}^y,-S_{i+1}^x,-S_{i+1}^z), \end{aligned} \tag{9}$$

in which T is the time-reversal operation, T_{na} denotes translation by n lattice sites, and I is spatial inversion with the inversion center at site 1, and $\hat{n}_1$ is given by

$$\hat{n}_1 = \frac{1}{\sqrt{2}}(1,-1,0)^{\mathrm{T}}. \tag{10}$$

The symmetry group G is generated by the operations in Eq. (9)

$$G = \langle T, R(\hat{z},\pi), R(\hat{n}_1,\pi)I, R(\hat{n}_1,\pi)T_a\rangle. \tag{11}$$

Notice in particular that the operations $T_{2a}, R(\hat{n}_2,\pi)I$ and $R(\hat{n}_2,\pi)T_a$ are also symmetries of the system where $\hat{n}_2 = \frac{1}{\sqrt{2}}(1,1,0)^{\mathrm{T}}$, which can be expressed in terms of the operations in Eq. (9) as $T_{2a} = [R(\hat{n}_1,\pi)T_a]^2$, $R(\hat{n}_2,\pi)I = R(\hat{z},\pi)\cdot R(\hat{n}_1,\pi)I$, $R(\hat{n}_2,\pi)T_a = R(\hat{z},\pi)\cdot R(\hat{n}_1,\pi)T_a$.

It is interesting to note the group structure of G. Since $\langle T_{2a}\rangle$ is an abelian normal subgroup of G, it is legitimate to consider the quotient group $G/\langle T_{2a}\rangle$. Notice that in the sense of modulo T_{2a}, all four generators of G in Eq. (11) square to the identity element and mutually commute, therefore

$$G/\langle T_{2a}\rangle \simeq (\mathbb{Z}_2)^4, \tag{12}$$

in which $\langle T, R(\hat{z},\pi), R(\hat{n}_1,\pi)I, R(\hat{n}_1,\pi)T_a\rangle/\langle T_{2a}\rangle \simeq (\mathbb{Z}_2)^4$. Namely, the symmetry group G has a nonsymmorphic structure, characterized by the following short exact sequence:

$$1 \to \langle T_{2a}\rangle \to G \to (\mathbb{Z}_2)^4 \to 1. \tag{13}$$

3. Exact solution of the model

The Hamiltonian in Eq. (1) can be exactly solved via the Jordan–Wigner transformation. In this section, we discuss the exact solution of the model and the resulting energy spectrum.

3.1. Jordan-Wigner transformation

In the Jordan–Wigner transformation, the spin-$\frac{1}{2}$ operators can be mapped onto spinless fermionic operators as

$$S_i^+ = c_i^\dagger T_i, \quad S_i^- = c_i T_i, \quad S_i^z = c_i^\dagger c_i - \frac{1}{2}, \tag{14}$$

where $c_i^\dagger$ creates a spinless fermion at site i, and $c_i^\dagger$ and c_j obey the canonical anticommutation relation

$$\{c_i^\dagger, c_j\} = \delta_{ij}, \tag{15}$$

and T_i is the Jordan–Wigner string

$$T_i = \mathrm{e}^{\mathrm{i}\pi\Sigma_{j=1}^{i-1} c_j^\dagger c_j}. \tag{16}$$

Notice that T_{N+1} is the fermion-parity operator, whose eigenvalues are ± 1. We impose the periodic boundary condition $S_{N+1}^a = S_1^a$, where N denotes the chain length (taken to be even throughout this work) and $a \in \{x,y,z\}$. Under the Jordan–Wigner transformation, the interaction at the boundary between sites N and 1 acquires an extra factor of T_{N+1}. Depending on the fermion parity, we impose the fermionic boundary condition

$$c_{N+1} = \sigma c_1, \qquad \sigma = \pm 1. \tag{17}$$

Consequently, a spin chain with periodic boundary conditions is mapped onto a fermionic chain whose boundary conditions are periodic (anti-periodic) in the even (odd) fermion-parity sector. In this section, we consider only the periodic fermionic boundary condition ($\sigma = 1$) for simplicity. Calculations for the anti-periodic boundary condition can be carried out in a similar manner.[60]

The Hamiltonian can be rewritten as the sum of contributions from odd and even bonds

$$\begin{aligned} H = & \sum_{i\in\text{odd}} \Big[K S_i^x S_{i+1}^x + J\left(S_i^x S_{i+1}^x + S_i^y S_{i+1}^y\right) \\ & + \Gamma\left(S_i^x S_{i+1}^y + S_i^y S_{i+1}^x\right)\Big] \\ & + \sum_{i\in\text{even}} \Big[K S_i^y S_{i+1}^y + J\left(S_i^x S_{i+1}^x + S_i^y S_{i+1}^y\right) \\ & + \Gamma\left(S_i^x S_{i+1}^y + S_i^y S_{i+1}^x\right)\Big]. \end{aligned} \tag{18}$$

Defining two sets of fermionic operators distinguished by the parity of the site index i

$$c_{2m} = b_m, \quad c_{2m-1} = a_m, \quad 1 \le m \le N/2, \tag{19}$$

we obtain the spinless fermion model after the Jordan–Wigner transformation as

$$\begin{aligned} H = & \frac{1}{4}\sum_i \big[(K+2J)a_i^\dagger b_i + (K-2\mathrm{i}\Gamma)a_i^\dagger b_i^\dagger \\ & + (K+2J)b_i^\dagger a_{i+1} - (K+2\mathrm{i}\Gamma)b_i^\dagger a_{i+1}^\dagger + \text{H.c.}\big]. \end{aligned} \tag{20}$$

Performing the following Fourier transformation (a is the lattice constant):

$$\begin{aligned} a_j &= \frac{1}{\sqrt{N/2}}\sum_k \mathrm{e}^{-\mathrm{i}k\cdot 2aj} a_k, \\ b_j &= \frac{1}{\sqrt{N/2}}\sum_k \mathrm{e}^{-\mathrm{i}k\cdot 2aj} b_k, \end{aligned} \tag{21}$$

the Hamiltonian can be expressed in terms of a_k, b_k and their Hermitian conjugates as

$$\begin{aligned} H &= \sum_{k>0,k\in K_\text{e}} H_k \\ &= \sum_{k>0,k\in K_\text{e}} \big[(A_k+B_k)a_k^\dagger b_k + (A_k-B_k)a_{-k}^\dagger b_{-k} \\ &\quad + (C_k+D_k)a_k^\dagger b_{-k}^\dagger + (C_k-D_k)a_{-k}^\dagger b_k^\dagger + \text{H.c.}\big], \end{aligned} \tag{22}$$

where the coefficients A_k, B_k, C_k, D_k are given by

$$\begin{aligned} A_k &= \frac{1}{4}(K+2J)(1+\cos k), \\ B_k &= \frac{\mathrm{i}}{4}(K+2J)\sin k, \\ C_k &= \frac{1}{4}\big[(K-2\mathrm{i}\Gamma)+(K+2\mathrm{i}\Gamma)\cos k\big], \\ D_k &= \frac{1}{4}(\mathrm{i}K-2\Gamma)\sin k. \end{aligned} \tag{23}$$

In Eq. (23), the lattice constant is set to $a = 1/2$ for simplicity.

The fermionic boundary condition Eq. (17) can be rewritten as

$$a_{N/2+1} = a_1. \tag{24}$$

This boundary condition restricts the allowed k-modes to a discrete set that depends on the parity of $N/2$. For the even case

$$K_\text{e} = \left\{ \frac{2\pi n}{Na} \,\middle|\, n = \pm1, \pm2, \ldots, \pm\frac{N}{4} \right\}, \tag{25}$$

and for the odd case

$$K_\text{e} = \left\{ \frac{2\pi n}{Na} \,\middle|\, n = 0, \pm1, \ldots, \pm\frac{1}{2}\left(\frac{N}{2}-1\right) \right\}. \tag{26}$$

Here the subscript "e" in K_e denotes the even-fermion-parity sector.

The Hamiltonian in Eq. (22) can be cast into the Bogoliubov–de Gennes (BdG) form

$$H = \sum_{k>0,k\in K_\text{e}} \Psi_k^\dagger H_\text{BdG}(k)\Psi_k, \tag{27}$$

where Ψ_k is the Nambu spinor defined as

$$\Psi_k = (a_k, b_k, a_{-k}^\dagger, b_{-k}^\dagger)^\text{T}, \tag{28}$$

and the 4×4 Bogoliubov–de Gennes matrix $H_\text{BdG}(k)$ is

$$H_\text{BdG}(k) = \begin{pmatrix} 0 & A_k+B_k & 0 & C_k+D_k \\ A_k^*+B_k^* & 0 & -C_k+D_k & 0 \\ 0 & -C_k^*+D_k^* & 0 & -A_k^*+B_k^* \\ C_k^*+D_k^* & 0 & -A_k+B_k & 0 \end{pmatrix}. \tag{29}$$

The BdG matrix satisfies particle–hole symmetry, meaning that there exists an anti-unitary operator $\mathcal{C}$ such that

$$\mathcal{C}H_\text{BdG}(k)\mathcal{C}^{-1} = -H_\text{BdG}(-k). \tag{30}$$

For the BdG matrix in Eq. (29), the operator $\mathcal{C}$ is given by

$$\mathcal{C} = P\mathcal{K}, \tag{31}$$

where $\mathcal{K}$ denotes complex conjugation, and P is a 4×4 unitary matrix acting in Nambu space, given by

$$P = \begin{pmatrix} 0&0&1&0 \\ 0&0&0&1 \\ 1&0&0&0 \\ 0&1&0&0 \end{pmatrix}. \tag{32}$$

The particle–hole symmetry guarantees that the eigenvalues of the BdG Hamiltonian come in positive-negative pairs; for example, if E is an eigenvalue at momentum k, then $-E$ is also an eigenvalue at momentum $-k$.

The BdG Hamiltonian in Eq. (29) also admits spatial inversion symmetry, meaning that there exists a unitary operator $\mathcal{I}$ such that

$$\mathcal{I}H_\text{BdG}(k)\mathcal{I}^{-1} = H_\text{BdG}(-k). \tag{33}$$

The corresponding 4×4 representation is

$$\mathcal{I}=\begin{pmatrix}0&1&0&0\\1&0&0&0\\0&0&0&1\\0&0&1&0\end{pmatrix}. \tag{34}$$

This symmetry ensures that the energy spectrum satisfies $E_l(k)=E_l(-k)$, where l denotes the band index.

By diagonalizing the BdG Hamiltonian (29), we obtain the energy spectra consisting of four branches $\{E_+(k),-E_+(-k),E_-(k),-E_-(-k)\}$, corresponding to the four eigenvalues of the matrix, where the dispersions are given by

$$E_\pm(k)\;=\;\left|\sqrt{\Delta(k)}\pm\frac{1}{2}|K\cos(k/2)|\right|, \tag{35}$$

in which

$$\Delta(k)\;=\;\Gamma^2\sin^2(k/2)+\left(J+\frac{K}{2}\right)^2\cos^2(k/2). \tag{36}$$

We denote by v_{lk} and u_{lk} $(l=\pm)$ the eigenvectors of $H_{\rm BdG}(k)$ corresponding to eigenvalues $E_l(k)$ and $-E_l(-k)$, respectively

$$\begin{aligned}H_{\rm BdG}(k)\,v_{lk}&=E_l(k)\,v_{lk},\\H_{\rm BdG}(k)\,u_{lk}&=-E_l(-k)\,u_{lk}.\end{aligned} \tag{37}$$

Defining the operators through

$$\gamma_{lk}^\dagger=\Psi_k^\dagger v_{lk},\qquad \beta_{lk}^\dagger=\Psi_k^\dagger u_{lk}, \tag{38}$$

from the particle–hole symmetry, we have

$$\beta_{lk}^\dagger=\gamma_{l,-k}. \tag{39}$$

Combining the k and $-k$ sectors into a single sum over the momentum set $K_{\rm e}$, the diagonalized Hamiltonian takes the compact form

$$H=\sum_{k\in K_{\rm e}}\sum_{l=\pm}E_l(k)\left(\gamma_{lk}^\dagger\gamma_{lk}-\tfrac{1}{2}\right). \tag{40}$$

The ground state $|GS\rangle$ is determined by the condition that it is annihilated by γ_{lk}, i.e.

$$\gamma_{lk}\,|GS\rangle=0. \tag{41}$$

However, we note that the ground state obtained directly from the Jordan–Wigner transformation is non-degenerate and thus does not capture the full set of ground states of the original spin model. This discrepancy arises from taking only $\sigma=1$ in the fermionic boundary condition in Eq. (17); considering only the periodic sector is insufficient. Both periodic and anti-periodic sectors must be included to recover the correct ground state degeneracy.

3.2. Gapless and gapped phases

To proceed, we fix $K=1$ as discussed in Section 2 and restrict our attention to the (J,Γ) plane. Notice that $\Delta(k)$ in Eq. (36) is consistent with the equivalence relations in Eqs. (5) and (8), and as a result, the dispersion in Eq. (35) is symmetric with respect to the $\Gamma=0$ and $J=-1/2$ lines in Fig. 1.

3.2.1. The gapless $\Gamma=0$ line

Along the $\Gamma=0$ line, the two points $J=0$ and $J=-1$ are special, where the Hamiltonian reduces to the pure Kitaev model, and $E_-(k)$ vanishes identically, leading to the presence of Majorana flat bands as illustrated in Fig. 1.

When $\Gamma=0$ and away from the aforementioned two special points, the spin Hamiltonian reduces to the Kitaev–XX model without the Γ interaction, and the energy dispersions in Eq. (35) always exhibit a zero point at the wave vector $k_{\rm F}=\pi$, as shown in Fig. 3(b). Expanding the dispersions around $k_{\rm F}$ with $q=k-k_{\rm F}$ gives two helical branches of Majorana fermions with distinct Fermi velocities. In the low-energy limit, namely in the vicinity of $k_{\rm F}=\pi$, both branches of the dispersion scale as

$$E(q)\sim q^z, \tag{42}$$

where $z=1$ is the dynamical critical exponent. Thus, along the $\Gamma=0$ line, the system is gapless and relativistic. The two low-energy dispersions in Eq. (42) define two Majorana fermions that exhibit an emergent Ising conformal symmetry, each associated with a corresponding set of Ising operator-product expansions (OPEs). Consequently, the low-energy theory consists of two branches of helical Majorana fermions whose combined central charge is $c=1$.

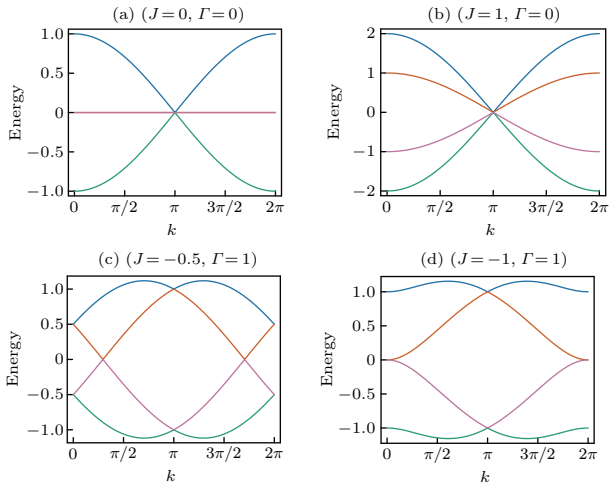


Fig. 3. Energy dispersions in the gapless phase for (a) $J=0$, $\Gamma=0$, (b) $J=1$, $\Gamma=0$, (c) $J=-0.5$, $\Gamma=1$, (d) $J=-1$, $\Gamma=1$.

We note that, as will be discussed in Subsection 3.2.3 and Subsection 4.1, the regions $(J>0,\Gamma>0)$, $(J>0,\Gamma<0)$, $(J<-1,\Gamma>0)$, and $(J<-1,\Gamma<0)$ are gapped and exhibit different magnetic orders. Therefore, the $(J>0,\ \Gamma=0)$ and

$(J<-1, \Gamma=0)$ lines are continuous phase transition lines separating distinct ordered phases, and hence are lines of deconfined quantum critical points beyond the conventional Landau paradigm of second-order phase transitions.[61–64]

3.2.2. The gapless $-1<J<0$ region

When $\Gamma \neq 0$, the gapless region is given by $-1<J<0$. In this parameter range, the dispersion always exhibits two zero-energy points located at momenta k_{F} and $2\pi - k_{\mathrm{F}}$, where

$$k_{\mathrm{F}} = 2\cos^{-1}\left(\sqrt{\frac{\Gamma^2}{\Gamma^2+|J(J+1)|}}\right). \tag{43}$$

As shown in Fig. 3(c), in the gapless phase $(-1<J<0)$, the low-energy dispersion is linear, giving rise to two helical branches of Majorana fermions with identical Fermi velocity but shifted in momentum. The dynamical critical exponent is $z=1$, with total central charge $c=1$.

3.2.3. The gapless $J=0$ and $J=-1$ lines with dynamical critical exponent $z=2$

On the phase transition lines at $J=-1$ and $J=0$ (except for the two special points with $\Gamma=0$ mentioned before), the low-energy spectrum has a quadratic dispersion, as shown in Fig. 3(d). Hence, the dynamical critical exponent is given by $z=2$. These two lines are phase boundaries separating the gapless $-1<J<0$ region from the gapped regions to be discussed in Subsection 3.2.4.

3.2.4. The gapped $(J>0, \Gamma>0)$ and its unitarily equivalent regions

The $(J>0, \Gamma>0)$ region has a gapped energy spectrum. Because of the equivalence relations in Eqs. (4) and (5), the regions $(J>0, \Gamma<0)$, $(J<-1, \Gamma>0)$, and $(J<-1, \Gamma<0)$ are also gapped. Hence, it is sufficient to focus on the $(J>0, \Gamma>0)$ region. The energy gap in this region can be summarized compactly as

$$\Delta_{\mathrm{g}} = \min\left\{J, \Gamma, \frac{\Gamma}{2}\sqrt{\tfrac{4D-1}{D}}\right\},$$
$$D = \left(J+\tfrac{1}{2}\right)^2 - \Gamma^2. \tag{44}$$

3.2.5. Implication for phase diagram

In summary, our analysis of dispersion relations and energy gaps implies that the (J, Γ) plane is naturally partitioned into six distinct phases: four gapped phases and two gapless phases, in accordance with Fig. 1. The vertical transition lines at $J=-1$ and $J=0$ separate the gapped and gapless regions, while the horizontal line at $\Gamma=0$ further divides the gapped region into four disconnected parts and the gapless region into two parts.

4. Phase diagram

In the previous section, we identified six independent phases in the (J, Γ) parameter space of the Kitaev–XX–Γ model. In this section, we turn to an investigation of the physical properties within each of these phases. To this end, we employ numerical DMRG simulations.

4.1. Ordered phase

4.1.1. Ground state degeneracy

As mentioned earlier, the ground state in the periodic sector of the Jordan–Wigner fermion does not capture all possible features of the original spin model. In particular, if the ground states of the system are degenerate, spontaneous symmetry breaking can occur, implying the existence of local order parameters. Therefore, the next step is to determine whether the ground state is degenerate.

In a finite-size system, there is an exponentially small energy splitting $\Delta(N)$ between the degenerate ground states, having the following scaling form:

$$\Delta(N) = A\,\mathrm{e}^{-N/\xi}, \tag{45}$$

where N is the system size, A is a constant, and ξ denotes the correlation length. In this case, the finite-size energy gap decreases exponentially with increasing chain length and eventually closes in the thermodynamic limit $(N\to\infty)$.

By contrast, the excitation gap, defined as the energy difference between the first excited state and the ground states, behaves as

$$\Delta_{\mathrm{e}}(N) = \Delta_\infty + B\,\mathrm{e}^{-N/\xi}, \tag{46}$$

where Δ_∞ represents the excitation gap in the thermodynamic limit, and B is a constant. Here, the gap converges to a finite value as the system size increases. Therefore, by observing the scaling behavior of the energy gap in DMRG simulations, we can distinguish between degenerate and non-degenerate ground states: if the gap tends to close exponentially rapidly with increasing N, the ground state is degenerate.

The simulation results in Fig. 4 are consistent with degenerate ground states. In the gapped phase, the finite-size energy gap exhibits exponential decay with system size. Specifically, Fig. 4(a) shows the gap between the first ground state and the lowest-lying orthogonal state. This splitting decreases rapidly and vanishes in the thermodynamic limit within numerical precision ($\sim 5\times10^{-14}$), demonstrating that the two states form a degenerate ground-state manifold. By contrast, Fig. 4(b) displays the gap between the first ground state and the second lowest-lying orthogonal state. This quantity converges to a finite value $\Delta_\infty \approx 0.9$, confirming that it corresponds to the true excitation gap of the system. Therefore, we conclude that the ground state in the $(J>0, \Gamma>0)$ phase is two-fold degenerate. We have also investigated other gapped phases, and the analysis indicates that their ground states are likewise two-fold

degenerate, which is expected due to the equivalence relations in Eqs. (5) and (8).

On the other hand, along the phase transition lines, the ground state is expected to be non-degenerate, and the excitation gap follows a power-law scaling

$$\Delta(N) \sim N^{-z}, \tag{47}$$

where the critical exponent z is defined as in Eq. (42). As shown in Figs. 4(c) and 4(d), we examine two representative points on the transition lines $\Gamma = 0$ ($z = 1$) and $J = -1$ ($z = 2$). Plotting the energy gap against $1/N^z$ yields a clear linear behavior, confirming the expected scaling form.

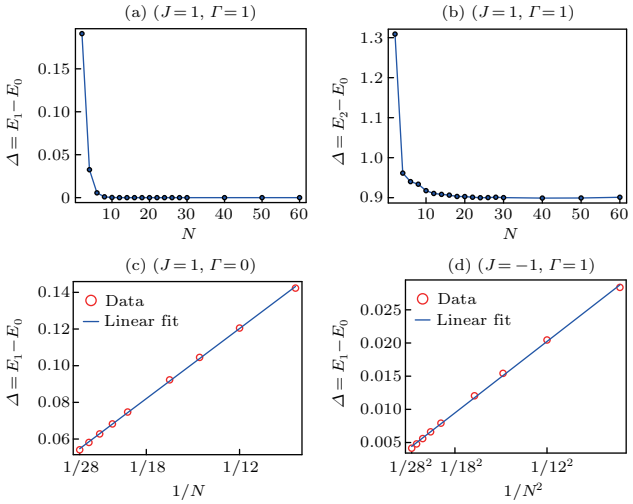


Fig. 4. (a) $E_1 - E_0$ vs. N at $(J = 1, \Gamma = 1)$, (b) $E_2 - E_0$ vs. N at $(J = 1, \Gamma = 1)$, (c) $E_1 - E_0$ vs. $1/N$ at $(J = 1, \Gamma = 0)$, (d) $E_1 - E_0$ vs. $1/N^2$ at $(J = -1, \Gamma = 1)$, where E_0, E_1, and E_2 represent the lowest, next-lowest, and third-lowest energies, respectively. The chain length N is varied from 2 to 60 in panels (a) and (b), and from 10 to 28 in panels (c) and (d). The maximum bond dimension m and truncation error ε in DMRG calculations are taken as $m = 1500$ and $\varepsilon = 10^{-12}$.

4.1.2. Correlation functions

We show that the system exhibits FM or AFM order along the $(1,1,0)$- or $(1,-1,0)$-directions, depending on the parameter region. In this subsection, correlation functions are investigated.

Define operators $\Lambda_i^{\pm}$ at site i as

$$\Lambda_i^{\pm} = S_i^x \pm S_i^y. \tag{48}$$

We examine the corresponding two-point correlation function

$$C^{\lambda}(r) = \langle \Lambda_i^{\lambda} \Lambda_{i+r}^{\lambda} \rangle, \tag{49}$$

where $\lambda = \pm$, and $\langle \cdots \rangle$ denotes the expectation value with respect to the ground state. If $C^{\lambda}(r)$ saturates to a finite value as $r \to \infty$, the system exhibits magnetic order characterized by Λ_i^{λ}.

The results of DMRG simulations for $C^{\lambda}(r)$ are shown in Fig. 5. In the $J > 0$ region, as illustrated in Fig. 5(a) (Fig. 5(b)), the correlation function $C^{+}(r)$ ($C^{-}(r)$) for $\Gamma > 0$ ($\Gamma < 0$) exhibits a staggered structure as a function of r, whereas $C^{-}(r)$ ($C^{+}(r)$) vanishes at large r. These behaviors indicate that the system develops antiferromagnetic (AFM) order along the $(1,1,0)$- and $(1,-1,0)$-directions, in the $(J > 0, \Gamma > 0)$ and $(J > 0, \Gamma < 0)$ regions, respectively. These two phases are denoted as AFM-I and AFM-II in the phase diagram in Fig. 1. The corresponding order parameters $\mathcal{O}_i^{\mathrm{s},\pm}$ are given by

$$\mathcal{O}_i^{\mathrm{s},\pm} = (-1)^i \left(S_i^x \pm S_i^y\right), \tag{50}$$

where '+' corresponds to the AFM-I phase and '−' to the AFM-II phase, and the superscript s in $\mathcal{O}_i^{\mathrm{s},\pm}$ denotes the staggered nature of the operator. Moreover, the equivalence relation in Eq. (5) implies that these two order parameters transform into each other via the global spin rotation $R(\hat{x}, \pi)$

$$U \mathcal{O}_i^{\mathrm{s},+} U^{\dagger} = \mathcal{O}_i^{\mathrm{s},-}, \tag{51}$$

where U denotes the unitary operator corresponding to $R(\hat{x}, \pi)$; this transformation can be straightforwardly verified.

In the $J < -1$ region, as illustrated in Figs. 5(c) and 5(d), the correlation functions $C^{-}(r)$ ($C^{+}(r)$) converge to a uniform nonzero value as $r \to \infty$ for $\Gamma > 0$ ($\Gamma < 0$). These two phases are denoted as FM-I and FM-II in the phase diagram in Fig. 1. The corresponding order parameters are

$$\mathcal{O}_i^{\pm} = S_i^x \pm S_i^y, \tag{52}$$

where '+' corresponds to $\Gamma < 0$ and '−' to $\Gamma > 0$. Furthermore, the equivalence relation in Eq. (8) implies that the AFM and FM order parameters can be transformed into each other via a two-sublattice rotation U_2' defined in Eq. (6)

$$U_2' \mathcal{O}_i^{\mathrm{s},\pm} U_2'^{\dagger} = \mathcal{O}_i^{\mp}, \tag{53}$$

which can be straightforwardly verified.

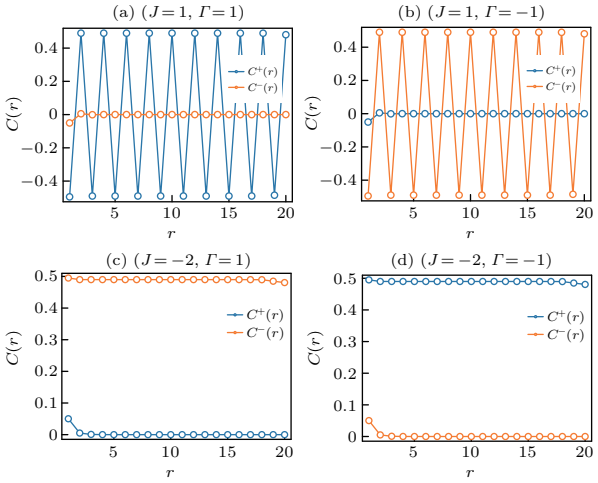


Fig. 5. Correlation functions $C^{\pm}(r)$ as a function of r for (a) $(J = 1, \Gamma = 1)$, (b) $(J = 1, \Gamma = -1)$, (c) $(J = -2, \Gamma = 1)$, and (d) $(J = -2, \Gamma = -1)$. DMRG simulations are performed on systems of $N = 100$ sites using open boundary conditions. The maximum bond dimension m and truncation error ε in DMRG calculations are taken as $m = 1500$ and $\varepsilon = 10^{-12}$.

It is worth noting that we evaluate the spin correlation functions numerically using DMRG; however, they can also be determined analytically via the Jordan–Wigner transformation. Under this transformation, spin operators acquire nonlocal string factors as given in Eq. (16). For the transverse components of the spin, these strings do not cancel completely, leaving behind a long product of Majorana fermion operators. Because the fermionic Hamiltonian is quadratic, the expectation value of this long Majorana chain can be reduced, through Wick's theorem, to the Pfaffian of an antisymmetric matrix constructed from two-point fermionic correlators. In a translation-invariant system, the matrix elements depend only on the relative separation of the sites involved, so the resulting Pfaffian is equivalent to the determinant of a Toeplitz or block-Toeplitz matrix. In the thermodynamic limit, these become infinite-dimensional Toeplitz determinants whose asymptotic behaviour governs the spin correlation functions at large distances.[65–67] The resulting analytical solution is expected to agree with our DMRG calculations.

4.1.3. Symmetry breaking patterns

We now analyze the symmetry-breaking patterns in the AFM-I and AFM-II phases. Analysis in the FM-I and FM-II phases can be carried out in a similar manner.

The symmetry generators of the Hamiltonian are given in Eq. (9). It can be verified that the unbroken symmetry groups $G_{\text{AFM-I}}$ and $G_{\text{AFM-II}}$ of the magnetic orders in the AFM-I and AFM-II phases are

$$\begin{aligned} G_{\text{AFM-I}} &= \langle T\cdot R(\hat{z},\pi),\ R(\hat{n}_2,\pi)T_a,\ R(\hat{n}_1,\pi)I\rangle, \\ G_{\text{AFM-II}} &= \langle T\cdot R(\hat{z},\pi),\ R(\hat{n}_2,\pi)I,\ R(\hat{n}_1,\pi)T_a\rangle. \end{aligned} \tag{54}$$

Using the group relations, one finds that two of the nonsymmorphic generators in Eq. (54) square to a two-site translation,

$$[R(\hat{n}_2,\pi)T_a]^2 = T_{2a}, \quad [R(\hat{n}_1,\pi)T_a]^2 = T_{2a}, \tag{55}$$

while the remaining generators square to the identity. Thus, the normal subgroup $\langle T_{2a}\rangle$ is contained in both $G_{\text{AFM-I}}$ and $G_{\text{AFM-II}}$. In the sense of modulo T_{2a}, all three generators of $G_{\text{AFM-I}}$ and $G_{\text{AFM-II}}$ in Eq. (54) square to the identity element and mutually commute, yielding the following quotient structure:

$$G_{\text{AFM-I}}/\langle T_{2a}\rangle \cong (\mathbb{Z}_2)^3, \quad G_{\text{AFM-II}}/\langle T_{2a}\rangle \cong (\mathbb{Z}_2)^3. \tag{56}$$

Since the Hamiltonian symmetry group satisfies $G/\langle T_{2a}\rangle \cong (\mathbb{Z}_2)^4$, the ground-state degeneracy in both AFM-I and AFM-II phases is

$$|(\mathbb{Z}_2)^4|/|(\mathbb{Z}_2)^3| = 2, \tag{57}$$

which agrees with the numerical results from the DMRG simulations discussed in Subsection 4.1.1. Thus, both AFM-I and AFM-II phases exhibit the following symmetry-breaking pattern:

$$(\mathbb{Z}_2)^4 \to (\mathbb{Z}_2)^3. \tag{58}$$

However, although the symmetry breaking in both AFM-I and AFM-II phases exhibits the structure $(\mathbb{Z}_2)^4 \to (\mathbb{Z}_2)^3$, the unbroken symmetry groups are distinct as shown in Eq. (54), indicating that these two phases are different within the framework of Landau symmetry-breaking theory.

4.1.4. Deconfined quantum critical line

To further confirm numerically the existence of the line of deconfined quantum critical points discussed in Subsection 3.2.1, we examine the long-distance correlation functions associated with the AFM-I and AFM-II order parameters using DMRG, defined as

$$C_{\text{s}}^{\pm}(N) = \langle \mathcal{O}_1^{\text{s},\pm}\mathcal{O}_N^{\text{s},\pm}\rangle. \tag{59}$$

Here, N denotes the chain length. Fixing the coupling J and varying Γ, we monitor the evolution of this correlation function. In the vicinity of a continuous quantum phase transition, the corresponding order parameter is expected to shrink continuously to zero without any discontinuous jumps when approaching the critical point.

Our numerical simulations, summarized in Fig. 6, are consistent with this expectation. The finite-size effects, as seen in Fig. 6, indicate that the spin correlation function becomes increasingly size-independent as N grows, and the curves for different system sizes gradually collapse onto a single profile. This behavior rules out discontinuous changes of the order parameters typical of a first-order transition and strongly suggests that the AFM-I to AFM-II transition is continuous, supporting the interpretation of this phase boundary as a candidate deconfined quantum critical line. A similar argument applies to the transition between the FM-I and FM-II phases.

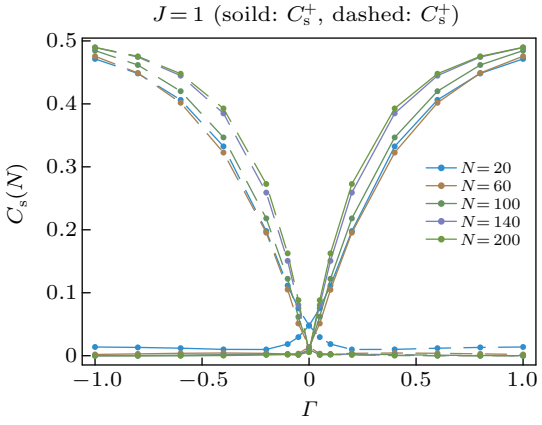


Fig. 6. The spin correlation function defined in Eq. (59) is evaluated for several chain lengths. The coupling is fixed at $J=1$, while Γ is varied from 1 to -1 in 11 uniform steps. The correlation distance is chosen as $r=N$. DMRG simulations are performed using open boundary conditions. The maximum bond dimension m and truncation error ε in the DMRG calculations are set to $m=1500$ and $\varepsilon=10^{-12}$, respectively.

4.1.5. Energy-field relation

To further confirm the nature of the ordered phases, we examine the energy-field relations. It is sufficient to focus on the FM-I phase, since the other phases are related to it by the unitary operators U and U_2' discussed previously. Specifically, we consider the response of the system to the following types of external fields:

$$\begin{aligned} &-\frac{1}{\sqrt{2}}h_{x+y}\sum_i\left(S_i^x+S_i^y\right),\\ &-\frac{1}{\sqrt{2}}h_{x-y}\sum_i\left(S_i^x-S_i^y\right),\\ &-h_x\sum_i S_i^x,\\ &-h_y\sum_i S_i^y, \end{aligned} \tag{60}$$

each of which is added individually to the Hamiltonian in Eq. (1). If the system exhibits long-range order, then an arbitrarily small field can induce a nonzero expectation value of the order parameter in the thermodynamic limit, and the relation between the change in ground-state energy and the applied field becomes linear in the small-field limit. We monitor the ground-state energy as a function of the applied fields to identify which field induces the strongest response.

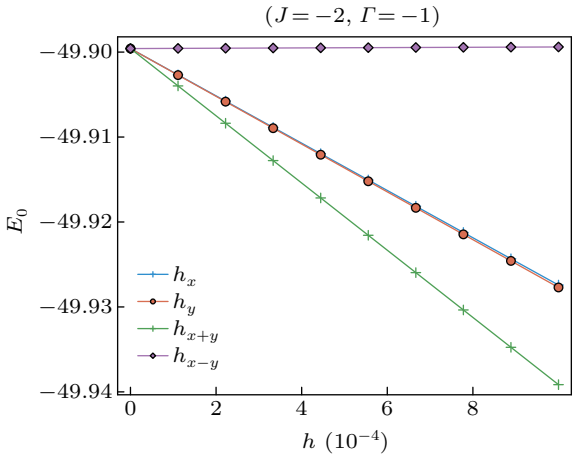


Fig. 7. Ground-state energy as a function of the applied fields. The field strength is varied from 0 to 10^{-3} in 10 uniform steps. DMRG simulations are performed in the FM-I phase with system size $N=80$ under open boundary conditions. The maximum bond dimension m and truncation error ε in DMRG calculations are taken as $m=1500$, $\varepsilon=10^{-12}$.

DMRG numerical results for all four types of fields in Eq. (60) are shown in Fig. 7. The responses to h_x and h_y collapse onto a common line and cannot be clearly distinguished. The ground-state energy responds linearly to all applied fields except h_{x-y}, which produces no response, as expected in the small-field regime. Among the different perturbations, the field applied along the $(1,1,0)$-direction, namely h_{x+y}, produces a larger response compared to the fields along the $(1,0,0)$- and $(0,1,0)$-directions corresponding to h_x and h_y. This confirms that the system develops FM order along the $(1,1,0)$-direction in the parameter region $(J<-2,\Gamma<0)$.

4.2. Gapless phase

As discussed in Subsection 3.2, the system is gapless within the range $-1\le J\le 0$. For brevity, we refer to the two gapless phases as gapless-I for $\Gamma>0$ and gapless-II for $\Gamma<0$, as shown in Fig. 1.

4.2.1. Central charge

When the low-energy physics is governed by a critical theory, the entanglement entropy $S(l)$ of a subregion of length l in a finite chain of total length N is predicted by conformal field theory (CFT) to scale as[68,69]

$$S(l)=\lambda\frac{c}{3}\ln(r_l)+\cdots, \tag{61}$$

where c is the central charge, $\lambda=1$ ($\lambda=1/2$) for periodic (open) boundary conditions,[70] and

$$r_l=\frac{N}{\lambda\pi}\sin\left(\frac{\pi l}{N}\right), \tag{62}$$

which reduces to l/λ in the limit $l\ll N$, and "$\cdots$" denotes subleading corrections. As discussed in Section 2, the phase transition line $\Gamma=0$ in Fig. 1 (except at the two special points $J=0$ and $J=-1$) realizes a critical theory described by a $c=1$ CFT, as do the two gapless phases.

Figure 8 shows DMRG results for $S(l)$ as a function of $\ln r_l$ at two representative points: $(J=1,\Gamma=0)$ on the transition line and $(J=-0.5,\Gamma=1)$ in the gapless-II phase. Under open boundary conditions, the entanglement entropy exhibits alternating oscillations, which are clearly visible in both panels of Fig. 8. To obtain precise estimates of the central charge, data points near the edges are discarded to reduce boundary effects. The fitted slopes yield central charge estimates of approximately $c\simeq 0.971$ at both representative points. With increasing system size N, these estimates are expected to converge to the theoretical value $c=1$.

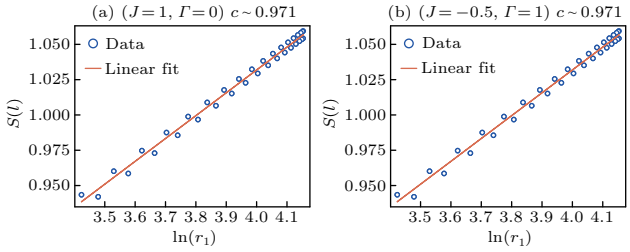


Fig. 8. Extraction of the central charge from a linear fit of the entanglement entropy $S(l)$ versus $\ln(r_l)$ at (a) $(J=1,\Gamma=0)$ and (b) $(J=-0.5,\Gamma=1)$. Here, $r_l=\frac{N}{\lambda\pi}\sin\left(\frac{\pi l}{N}\right)$, and the outermost 15% of data points near the edges are discarded to reduce boundary effects. DMRG simulations are performed on an open chain with $N=100$ sites. The maximum bond dimension and truncation error are set to $m=1500$ and $\varepsilon=10^{-12}$, respectively.

4.2.2. Correlation functions

Next, we examine the two-point spin correlation functions within the gapless phases. It is sufficient to focus on the

gapless-I phase, since the equivalence relation in Eq. (5) ensures that the two gapless phases are related by the spin rotation $R(\hat{x},\pi)$. Figure 9 shows the DMRG numerical results for $C^+(r)$ and $C^-(r)$ at a representative point $(J=-0.7,\Gamma=1)$, where $C^{\pm}(r)$ is defined in Eq. (49). It is evident that both $C^-(r)$ and the envelope of $C^+(r)$ exhibit oscillations with a wave vector that is incommensurate with the underlying lattice. These behaviors are consistent with the exact solutions presented in Subsection 3.2.2 for the gapless phase, where the wave vector $k_{\rm F}$ in Eq. (43) is generically incommensurate for arbitrary (J,Γ), except at special points.

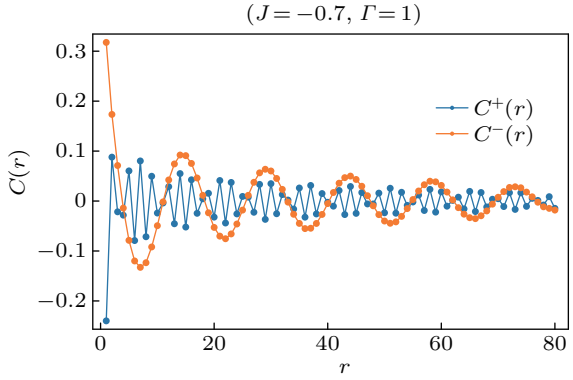


Fig. 9. Two-point spin correlation functions $C^+(r)$ and $C^-(r)$ as a function of site separation r at a representative point $(J=-0.7,\Gamma=1)$ in the gapless-I phase. DMRG simulations are performed on a chain of $N=100$ sites with open boundary conditions. The maximum bond dimension and truncation error are set to $m=1500$ and $\varepsilon=10^{-12}$, respectively.

5. Summary

In this work, we have investigated the ground-state properties of the exactly solvable spin-1/2 Kitaev–XX–Γ chain. Combining analytical methods based on the Jordan–Wigner transformation with large-scale DMRG simulations, we identify six distinct phases: four gapped phases exhibiting ferromagnetic or antiferromagnetic long-range order, and two gapless phases characterized by helical Majorana fermions at low energies. The gapped phases possess a two-fold degenerate ground-state manifold, whereas the gapless phases are described by a conformal field theory with central charge $c=1$. The system hosts rich quantum critical phenomena, including lines of deconfined quantum critical points with dynamical exponent $z=1$ and quadratic critical points with $z=2$, reflecting the intricate interplay between symmetry, magnetic order, and quantum fluctuations.

Appendix A: Majorana operators

Majorana zero modes appear at the zero-energy points $E_l(k_{\rm F})=0$. We define the corresponding Majorana operators as

$$\alpha^{(1)}_{lk} = \frac{1}{\sqrt{2}}\left(\gamma_{lk}+\gamma^{\dagger}_{l,-k}\right), \tag{A1}$$

$$\alpha^{(2)}_{lk} = \frac{1}{\sqrt{2}\mathrm{i}}\left(\gamma_{lk}-\gamma^{\dagger}_{l,-k}\right). \tag{A2}$$

These operators satisfy the Majorana condition in momentum space

$$(\alpha^{m}_{lk})^{\dagger} = \alpha^{m}_{l,-k}, \tag{A3}$$

and obey the canonical anticommutation relations

$$\{\alpha^{m}_{lk},\alpha^{m'}_{l'k'}\} = \delta_{ll'}\,\delta_{mm'}\,\delta_{kk'}. \tag{A4}$$

In terms of these operators, the Hamiltonian reads

$$H = \sum_{k\in K_{\rm e}}\sum_{l=\pm}\mathrm{i}E_l(k)\,\alpha^{(1)}_{lk}\alpha^{(2)}_{lk}. \tag{A5}$$

The Heisenberg equation of motion gives

$$[H,\alpha^{(1)}_{lk}] = -\mathrm{i}E_l(k)\,\alpha^{(2)}_{lk},\ [H,\alpha^{(2)}_{lk}] = +\mathrm{i}E_l(k)\,\alpha^{(1)}_{lk}. \tag{A6}$$

At zero-energy points $E_l(k_{\rm F})=0$, the corresponding Majorana operators commute with the Hamiltonian and thus define Majorana zero modes that are stationary in time.

Appendix B: Proof of the existence of zero-energy points in the gapless region

For $\Gamma\neq 0$, we first determine the gapless regions. The condition for $E_-(k_{\rm F})$ to vanish is

$$E_-(k_{\rm F})=0. \tag{B1}$$

Squaring the dispersion in Eq. (35) and rearranging terms yields

$$\Gamma^2\sin^2(k/2)+J(J+1)\cos^2(k/2)=0. \tag{B2}$$

Since $\sin^2(k/2),\cos^2(k/2)\geq 0$ and $\Gamma^2>0$, a necessary condition for Eq. (B1) to have a solution is

$$J(J+1)\leq 0, \tag{B3}$$

which gives the constraint

$$-1\leq J\leq 0. \tag{B4}$$

Equation (B1) can be further rewritten as

$$\Gamma^2+\left[J(J+1)-\Gamma^2\right]\cos^2(k/2)=0, \tag{B5}$$

leading to

$$0<\cos^2(k/2)=\frac{\Gamma^2}{\Gamma^2+|J(J+1)|}<1. \tag{B6}$$

Therefore, within the region $-1\leq J\leq 0$, the dispersion $E_-(k)$ always exhibits zero-energy points at wave vectors $k_{\rm F}$ and $2\pi-k_{\rm F}$, given explicitly by

$$k_{\rm F}=2\cos^{-1}\left(\sqrt{\frac{\Gamma^2}{\Gamma^2+|J(J+1)|}}\right). \tag{B7}$$

Appendix C: Proof of the energy gap in the $(J > 0, \Gamma > 0)$ region

In the region $(J > 0, \Gamma > 0)$, the lower branch of the spectrum can be written as

$$E_-(u) = \sqrt{\Gamma^2 + Du^2} - \frac{u}{2}, \tag{C1}$$

where

$$D = \left(J + \frac{1}{2}\right)^2 - \Gamma^2, \tag{C2}$$

$$u = |\cos(k/2)|. \tag{C3}$$

To determine the energy gap, we consider two scenarios.

(i) Minimum in the interior $u_0 \in (0,1)$: The stationary point u_0 satisfies $E'_-(u_0) = 0$, giving

$$0 < u_0^2 = \frac{\Gamma^2}{4D^2 - D} < 1, \tag{C4}$$

which requires

$$4D^2 - D > \Gamma^2. \tag{C5}$$

In this case, the energy gap is

$$\Delta_g = \frac{\Gamma}{2}\sqrt{\frac{4D-1}{D}}. \tag{C6}$$

(ii) Minimum at the boundary $u_0 = 0$ **or** $u_0 = 1$: The gap is given by

$$\Delta_g = \min\left\{E_-(u=0), E_-(u=1)\right\} = \min\{\Gamma, J\}. \tag{C7}$$

Combining both possibilities, the energy gap in the $(J > 0, \Gamma > 0)$ region can be summarized as

$$\Delta_g = \min\left\{J, \Gamma, \frac{\Gamma}{2}\sqrt{\frac{4D-1}{D}}\right\}. \tag{C8}$$

Data availability statement

The data that support the findings of this study are openly available in Science Data Bank at the following link https://doi.org/10.57760/sciencedb.j00113.00281.

Acknowledgments

This work is supported by the National Natural Science Foundation of China (Grant No. 12474476) and the Fundamental Research Funds for the Central Universities. DMRG calculations were performed using the ITensor software package.[71] Numerical data reported in this work are available from the authors upon request.

References

[1] Nussinov Z and van den Brink J 2015 *Rev. Mod. Phys.* **87** 1
[2] Brzezicki W, Dziarmaga J and Oleś A M 2007 *Phys. Rev. B* **75** 134415
[3] You W L and Tian G S 2008 *Phys. Rev. B* **78** 184406
[4] Eriksson E and Johannesson H 2009 *Phys. Rev. B* **79** 224424
[5] Sun K W and Chen Q H 2009 *Phys. Rev. B* **80** 174417
[6] Mahdavifar S 2010 *Eur. Phys. J. B* **77** 77
[7] Motamedifar M, Mahdavifar S and Shayesteh S F 2011 *J. Supercond. Nov. Magn.* **24** 769
[8] Jafari R 2011 *Phys. Rev. B* **84** 035112
[9] You W L 2012 *Eur. Phys. J. B* **85** 83
[10] Liu G H, Li W and You W L 2012 *Eur. Phys. J. B* **85** 168
[11] Liu G H, Li W, You W L, Tian G S and Su G 2012 *Phys. Rev. B* **85** 184422
[12] You W L, Horsch P and Oleś A M 2014 *Phys. Rev. B* **89** 104425
[13] Aziziha M, Motamedifar M and Mahdavifar S 2013 *Acta Phys. Pol. B* **44** 221
[14] Jafari R 2016 *J. Phys. A: Math. Theor.* **49** 185004
[15] You W L 2017 *Phys. Rev. B* **95** 224404
[16] Laurell P, Alvarez G and Dagotto E 2023 *Phys. Rev. B* **107** 104414
[17] Xu J L, Geng H, Wahab A, Yang X S, Xie Y E and Chen Y P 2025 *Chin. Phys. B* **34** 068401
[18] Luo Q, Zhao J Z and Wang X Q 2025 *Chin. Phys. Lett.* **42** 027501
[19] Chaloupka J, Jackeli G and Khaliullin G 2010 *Phys. Rev. Lett.* **105** 027204
[20] Winter S M, Riedl A, Kaib D, Valentí R and Honecker A 2017 *J. Phys.: Condens. Matter* **29** 493002
[21] Nishimoto S, Yushankhai V, Kondov S F, Mazin I, Li Y and Valentí R 2015 *Phys. Rev. B* **92** 184429
[22] Winter S M, Li Y, Jeschke H O and Valentí R 2016 *Phys. Rev. B* **93** 214431
[23] Wang W, Dong Z Y, Yu S L and Li J X 2017 *Phys. Rev. B* **96** 115103
[24] Gohlke J, Wachtel G, Yamaji Y, Pollmann F and Kim Y B 2018 *Phys. Rev. B* **97** 075126
[25] Winter S M, Kaib D and Valentí R 2019 *Phys. Rev. B* **100** 045150
[26] Kheiri S, Cheraghi H, Mahdavifar S and Sedlmayr N 2024 *Phys. Rev. B* **109** 134303
[27] Zhao Z, Yi T C, Xue M and You W L 2022 *Phys. Rev. A* **105** 063306
[28] Liu Z A, Dong Y L, Wu N, Wang Y and You W L 2021 *Physica A* **579** 126122
[29] Liu Z A, Yi T C, Sun J H, Dong Y L and You W L 2020 *Phys. Rev. E* **102** 032127
[30] Mahdavifar S and Liu D C 2024 *Sci. Rep.* **14** 30024
[31] Abbasi M, Mahdavifar S and Motamedifar M 2025 *Sci. Rep.* **15** 20469
[32] Abbasi M, Mahdavifar S and Motamedifar M 2025 *SciPost Phys. Core* **8** 001
[33] Jin X, Xue M, Zhao Z and You W L 2025 *Phys. Rev. E* **111** 014110
[34] Kitaev A 2006 *Ann. Phys. (N. Y.)* **321** 2
[35] Nayak C, Simon S H, Stern A, Freedman M and Das Sarma S 2008 *Rev. Mod. Phys.* **80** 1083
[36] Jackeli G and Khaliullin G 2009 *Phys. Rev. Lett.* **102** 017205
[37] Trebst S 2022 *Phys. Rep.* **950** 1
[38] Yang W, Nocera A, Herringer P, Raussendorf R and Affleck I 2022 *Phys. Rev. B* **105** 094432
[39] Luo Q, Zhao J, Wang X and Kee H Y 2021 *Phys. Rev. B* **103** 144423
[40] Catuneanu A, Sørensen E S and Kee H Y 2019 *Phys. Rev. B* **99** 195112
[41] Sørensen E S, Gordon J, Riddell J, Wang T and Kee H Y 2023 *Phys. Rev. Res.* **5** L012027
[42] Yang W, Xu C, Ma S, Nocera A and Affleck I 2025 *Phys. Rev. B* **112** 035104
[43] Yang W, Xu C, Xu S, Nocera A and Affleck I 2024 *Phys. Rev. B* **109** L180403
[44] Yang W, Nocera A, Xu C and Affleck I 2024 *SciPost Phys.* **17** 097
[45] Yang W, Nocera A, Tummuru T, Kee H Y and Affleck I 2020 *Phys. Rev. Lett.* **124** 147205
[46] Yang W, Nocera A, Xu C, Adhikary A and Affleck I 2025 *Phys. Rev. B* **111** 174414
[47] Yang W, Nocera A and Affleck I 2020 *Phys. Rev. B* **102** 134419
[48] Yang W, Nocera A, Sørensen E S, Kee H Y and Affleck I 2021 *Phys. Rev. B* **103** 054437
[49] Luo Q, Hu S and Kee H Y 2021 *Phys. Rev. Research* **3** 033048
[50] Sørensen E S, Catuneanu A, Gordon J and Kee H Y 2021 *Phys. Rev. X* **11** 011013
[51] Gordon J S, Catuneanu A, Sørensen E S and Kee H Y 2019 *Nat. Commun.* **10** 2470

[52] You W L, Sun G, Ren J, Yu W C and Oleś A M 2020 *Phys. Rev. B* **102** 144437

[53] Agrapidis C E, van den Brink J and Nishimoto S 2019 *Phys. Rev. B* **99** 224418

[54] Agrapidis C E, van den Brink J and Nishimoto S 2018 *Sci. Rep.* **8** 1815

[55] Sela E S, Jiang H C, Gerlach M H and Trebst S 2014 *Phys. Rev. B* **90** 035113

[56] Yang W, Nocera A and Affleck I 2020 *Phys. Rev. Research* **2** 033268

[57] Yang W, Xu C, Nocera A and Affleck I 2022 *Phys. Rev. B* **106** 064425

[58] Gruenewald J H, Kim J, Kim H S, Johnson J M, Hwang J, Souri M, Terzic J, Chang S H, Said A, Brill J W, Cao G, Kee H Y and Seo S S A 2017 *Adv. Mater.* **29** 163798

[59] Morris C M, Desai N, Viirok J, Hüvonen D, Nagel U, Rõom T, Krizan J W, Cava R J, McQueen T M, Koohpayeh S M, Kaul R K and Armitage N P 2021 *Nat. Phys.* **17** 832

[60] Wu N, Sedrakyan A and Essler F 2021 *Phys. Rev. B* **103** 094304

[61] Senthil T, Vishwanath A, Balents L, Sachdev S and Fisher M P A 2004 *Science* **303** 1490

[62] Senthil T, Balents L, Sachdev S, Vishwanath A and Fisher M P A 2004 *Phys. Rev. B* **70** 144407

[63] Sandvik A W 2007 *Phys. Rev. Lett.* **98** 227202

[64] Shao H, Guo W and Sandvik A W 2016 *Science* **352** 213

[65] Montroll E W, Potts R B and Ward J C 1963 *J. Math. Phys.* **4** 308

[66] Lieb E, Schultz T and Mattis D 1961 *Ann. Phys.* **16** 407

[67] Barouch E and McCoy B M 1971 *Phys. Rev. A* **3** 786

[68] Calabrese P and Cardy J 2009 *J. Phys. A* **42** 504005

[69] Ejima S, Bhaseen M J, Hohenadler M, Essler F H L, Fehske H and Simons B D 2011 *Phys. Rev. Lett.* **106** 015303

[70] Laflorencie N, Sørensen E S, Chang M S and Affleck I 2006 *Phys. Rev. Lett.* **96** 100603

[71] Fishman M, White S R and Stoudenmire E M 2022 *SciPost Phys. Codebases* **4**